

1 **Estimating Vertical Motion Profile Top-heaviness: Reanalysis compared to**  
2 **Satellite-based Observations and Stratiform rain fraction**

3 Larissa E. Back\* and Zachary Hansen and and Zachary Handlos

4 *Department of Atmospheric & Oceanic Sciences, University of Wisconsin, Madison, Wisconsin*

5 \**Corresponding author address:* Larissa E. Back, Department of Atmospheric & Oceanic Sciences,

6 University of Wisconsin, 1225 W. Dayton St., Madison, WI 53706

7 E-mail: lback@wisc.edu

## ABSTRACT

8 A method for representing geographic variability in vertical motion profile  
9 top-heaviness in reanalysis data is introduced. The results from this method  
10 are compared to a satellite-based method for estimating top-heaviness of verti-  
11 cal motion profiles over the oceans. The satellite-based method utilizes basis  
12 functions, idealized or from reanalysis, along with scatterometer wind con-  
13 vergence data and rainfall to estimate the top-heaviness of the vertical motion  
14 profile. Results from the two methods of estimating top-heaviness are signifi-  
15 cantly correlated. Both estimates of top-heaviness are compared to stratiform,  
16 shallow and convective rain fraction. Findings show geographic variability  
17 in stratiform rain fraction is not well correlated with estimated profile top-  
18 heaviness. Shallow rain fraction is not variable enough to explain this finding.  
19 The results may be due to geographic variations in the shape of convective or  
20 stratiform heating profiles. An example is given of how variations in convec-  
21 tive heating profiles could lead to a region with more stratiform rain having a  
22 more bottom-heavy profile.

## 23 1. Background

24 Tropical large-scale vertical motion profiles are important for a wide variety of dynamics prob-  
25 lems. However, they are difficult to measure, simulate and estimate, and basic science questions  
26 about what controls profile shape, or “top-heaviness” remain to be determined. The term ”top-  
27 heaviness” in this work is used to refer to the extent to which vertical motion peaks in the upper  
28 troposphere compared to lower in the troposphere. In this work, we compare climatological verti-  
29 cal motion profile shapes (top-heaviness) estimated from the ERA-interim reanalysis to satellite-  
30 based estimates of top-heaviness, as well as the fraction of rain that falls as stratiform, shallow  
31 and convective rain. We find that stratiform and shallow rain fraction do not explain geographic  
32 variability in vertical motion profiles and discuss why this may be the case.

33 Vertical motion profiles and latent heating profiles are closely intertwined, as can be seen from  
34 the dry static energy budget (e.g. Yanai et al. 1973; Handlos and Back 2014). Temperature ten-  
35 dencies on longer-than-diurnal timescales and horizontal advection are small in the tropics due to  
36 the large Rossby radius and gravity waves quickly distributing heating anomalies (Charney 1963;  
37 Bretherton and Smolarkiewicz 1989; Sobel and Bretherton 2000). Hence, the dominant balance in  
38 the energy budget is between vertical advection of dry static energy and “apparent heating” which  
39 consists of heating due to radiation, the release of latent heating by condensation and vertical con-  
40 vergence of the vertical eddy transport of sensible heat. The latter term is primarily important in  
41 the sub-cloud layer and latent heating is more variable than radiative heating. Hence, we can think  
42 of the vertical profile of latent heating as closely tied to vertical profile of vertical motion.

43 A number of studies have looked at the response of the circulation to variations in latent heating  
44 profile shape and shown that these variations have an impact on the large-scale circulation (e.g.  
45 Hartmann et al. 1984; Wu et al. 2000; Schumacher et al. 2004) when latent heating profile varia-

46 tions are imposed in numerical models. This suggests that simulating these correctly is critical to  
47 simulations of large-scale tropical circulations.

48 More recently, energetic frameworks for thinking about mean ITCZ shifts have gained popularity  
49 (e.g. Kang et al. 2009; Frierson et al. 2013; Schneider et al. 2014). This approach can even be  
50 generalized to zonally varying ITCZ shifts (Adam et al. 2016). In these frameworks, quantities  
51 related to the gross moist stability are critical to determining the size of the response of the ITCZ  
52 to extratropical forcing, or how far off the equator the ITCZ is located. The vertical structure of  
53 convection has a strong influence on the gross moist stability (e.g. Back and Bretherton 2006),  
54 so the vertical motion and latent heating profile of the convection influences where the ITCZ is  
55 in these theories. This provides added motivation for documenting and understand controls on  
56 vertical motion profiles.

57 Other recent work has suggested that the extent to which bottom-heavy circulations are simu-  
58 lated may influence modeled climate sensitivity (Sherwood et al. 2014). This correlation supports  
59 analyzing where bottom-heavy circulations exist in nature, using satellite or other data.

60 In this work, we introduce a principal component analysis-based method for examining the  
61 climatological shape of vertical motion profiles in reanalysis in section 2. We also use satellite  
62 data to estimate vertical motion profile shape (2a). We compare to Tropical Rainfall Measurement  
63 Mission (TRMM) climatological estimates of stratiform and shallow rain fraction and look at the  
64 relationship between the top-heaviness metrics and these quantities (2b). We discuss possible  
65 reasons for the lack of relationship we see in section 3. Finally, we summarize our conclusions in  
66 section 4.

## 67 2. Analysis

68 We perform a principal component analysis of vertical motion using monthly mean pressure  
69 level data from the ERA-interim reanalysis (Dee et al. 2011) for 2001 through 2006. The analysis  
70 is performed by placing each gridpoint-month corresponding to ocean regions at a latitude less  
71 than 20 degrees into a large space-agnostic matrix. Then, we perform the analysis in such a way  
72 that it produces empirical orthogonal functions (EOFs) that have vertical motion as a function of  
73 height and principal components which are functions of space and time.

74 The first two EOFs of vertical motion are shown in Figure 1a and explain 71.2 and 15.8 percent  
75 of the variance. They have been normalized as described below. They are statistically distinct  
76 from each-other and the third EOF by North et al. criteria (North et al. 1982). The first EOF  
77 is associated with deep vertical motion (or subsidence) extending throughout the troposphere.  
78 The second EOF corresponds to upward (downward) vertical motion in the upper troposphere  
79 and subsidence (ascent) in the lower troposphere. The sign of the vertical motion in the second  
80 EOF switches around 650hPa. The signs in the analysis have been chosen to have positive values  
81 corresponding to descent in the upper troposphere. The EOFs in Figure 1a are invariant in space  
82 and time and were scaled/normalized to make:

$$\frac{\int_{100hPa}^{1000hPa} \Omega_i(p)^2 dp}{900hPa} = 1 \quad (1)$$

83 This scaling choice affects the numerical values shown in Figures 1b, 2 and 3, but not the patterns  
84 (e.g. a different scaling choice would multiply all numbers given by the same constant).

85 Vertical motion can be approximated using the results of this principal component analysis.  
86 Following the notation of Back and Bretherton (2009b) we approximate the vertical motion:

$$\omega(x, y, p, t) = o_1(x, y, t)\Omega_1(p) + o_2(x, y, t)\Omega_2(p) \quad (2)$$

87 where  $\Omega_1(p)$  and  $\Omega_2(p)$  correspond to the EOFs shown in Figure 1 and the associated principal  
88 components are denoted  $o_1(x,y,t)$  and  $o_2(x,y,t)$ . The  $o_1(x,y,t)$  and  $o_2(x,y,t)$  can alternatively  
89 be described as the amplitudes of the EOFs. This latter interpretation will be used to estimate  
90 them from satellite observations in the method described below. In this framework, under the  
91 assumption of two vertical modes, and once scaling choices are made for  $\Omega_i$ , the shape of the  
92 vertical motion profile at a given location and time is a function of the ratio of  $o_2(x,y,t)$  to  $o_1(x,y,t)$   
93 only. Figure 1b shows examples of vertical motion profiles constructed from the EOFs shown in  
94 Figure 1 with a varying  $o_2/o_1$  ratio. The vertical motion profiles shown are all normalized the  
95 same way as the basis functions were, as in equation 1. Varying  $o_1$  and keeping the  $o_2/o_1$  ratio  
96 the same keeps the shape of the vertical motion profile the same (e.g. upward velocity at one level  
97 relative to another is the same), but varies the magnitude of vertical motion at each level.

98 Figure 2 shows a global map of the ratio of reanalysis  $o_2(x,y,t)/o_1(x,y,t)$ , the amplitude of the  
99 second function (the second principal component,  $o_2$ ) to the amplitude of the first function (first  
100 principal component,  $o_1(x,y,t)$ ) in regions where the amplitude of time-mean  $o_1$  corresponds to  
101 upward vertical motion ( $o_1 < 0$  following sign conventions in Figure 1a and equation 2.). The ratio  
102 is shown in only regions with upward vertical motion because we are focusing on deep convective  
103 regions. The average of the numerator and denominator are calculated separately before the ratio  
104 is calculated to be consistent with Figure 1b, so that the colors on this figure correspond to the  
105 ratios shown in Figure 1b. The map can be thought of as a global map of top-heaviness. Blue  
106 regions correspond to more bottom-heavy circulations and red regions correspond to more top-  
107 heavy circulations. Note the strong contrast in the global map of vertical motion profile top-  
108 heaviness between the top-heavy vertical motion profiles of the western Pacific warm pool and  
109 the more bottom-heavy vertical motion profiles seen in the central and eastern Pacific and Atlantic  
110 inter-tropical convergence zones.

111 *a. Satellite Omega Analysis*

112 Substantial uncertainties exist in reanalysis vertical motion profiles, which are not directly con-  
 113 strained by observations. Thus, it is desirable to have a way to estimate vertical motion profile  
 114 top-heaviness that does not depend directly on reanalysis. Luckily, the amplitudes of  $o_1$  and  $o_2$   
 115 can be estimated from satellite data using the methodology of Handlos and Back (2014), hereafter  
 116 HB. In HB's method, the top-heaviness ratio can have some dependence on reanalysis-derived ba-  
 117 sis functions (Figure 1a). However, HB also utilized idealized basis functions, as will this work, to  
 118 mitigate this issue. The reanalysis EOFs likely give our best estimate of basis functions, while the  
 119 idealized basis functions can be used to test the sensitivity of the results to basis function. In this  
 120 work, we follow the methodology described in HB for estimating vertical motion profile shape us-  
 121 ing satellite data; spatial and temporal resolution of the data are described in HB, as are estimates  
 122 of uncertainties. Satellite data comes from estimates of surface convergence (from QuikSCAT),  
 123 precipitation (TRMM 3B42, TRMM 2016a) and radiative cooling (NEWS Grecu and Olson 2006;  
 124 Grecu et al. 2009; L'Ecuyer and Stephens 2003, 2007; L'ecuyer and Mcgarragh 2010).

125 The concept behind the HB method utilizes the relationship between vertical motion, surface  
 126 convergence and precipitation. Assuming that vertical motion can be described by equation 2, and  
 127 neglecting some small terms, the dry static energy budget can be used to relate vertical motion and  
 128 precipitation via the following equation (equation (7) from HB):

$$LP(x, y, t) = M_{s1}o_1(x, y, t) + M_{s2}o_2(x, y, t) - \Delta F_{rad}(x, y, t) \quad (3)$$

129 where  $\Delta F_{rad}$  is the column-integrated radiative cooling,  $LP$  is the latent heating associated with  
 130 precipitation and gross dry stratifications  $M_{s1}$  and  $M_{s2}$  are denoted:

$$M_{si} = \int_{p_0}^{p_i} \Omega_i \frac{\partial s}{\partial p} \frac{dp}{g}; i = 1, 2. \quad (4)$$

131 In this equation,  $s = C_p T + gz$  is the dry static energy,  $p_0$  is 1000hPa and  $p_t$  is 100hPa and other  
 132 terms have their conventional meteorological meanings. Gross dry stratifications are calculated  
 133 from the mean  $s$  profile over the tropical oceans (in reanalysis), so these are assumed constant.

134 We wish to estimate  $o_2$  and  $o_1$  from satellite data, so another constraint is needed. For this we  
 135 utilize surface convergence from QuikSCAT. This can be related to the amplitude of  $o_i$  via the  
 136 following equation (HB equation (10)):

$$\nabla \cdot \vec{V}_{sfc}(x, y, t) = c_1 o_1(x, y, t) + c_2 o_2(x, y, t) \quad (5)$$

137 where  $c_i$  are constants derived from  $\Omega_i$ :

$$c_i = \frac{\Omega_i(975hPa) - \Omega_i(1000hPa)}{25hPa} \quad (6)$$

138 These constants represent the amount of surface convergence per unit amplitude of vertical motion  
 139 associated with the two basis functions.

140 The system of equations (3 and 5), combined with the satellite data has two unknowns  $o_1$  and  
 141  $o_2$ . Thus, we can solve for the shape of the vertical motion profile from the satellite data, either  
 142 using the reanalysis-determined basis functions, or any other basis functions we choose. The basis  
 143 functions are only used to calculate  $M_{si}$  and  $c_i$ .

144 Figure 3a shows the top-heaviness ratio ( $o_2/o_1$ ) as estimated from satellite data using this  
 145 methodology and the reanalysis-derived basis functions in regions where time-mean  $o_1$  corre-  
 146 sponds to upward vertical motion. Many of the broad-scale features are similar between Figure 2  
 147 and Figure 3a, but there are disagreements on smaller scales. As in Figure 2, the eastern Pacific  
 148 and Atlantic have more bottom-heavy vertical motion profiles, while the western Pacific and In-  
 149 dian ocean have more top-heavy ratios. The most top-heavy region is in the Bay of Bengal in both  
 150 cases. However, in the satellite data there is an asymmetry between the top-heaviness of the north-  
 151 ern and southern part of the western Pacific ITCZ, with the northern part being more top-heavy.

152 The details of which regions within the eastern Pacific and Atlantic are most bottom-heavy are also  
153 different. For example, in Figure 2 there are notable north-south gradients in bottom-heaviness in  
154 the eastern Pacific and Atlantic which are absent in Figure 3a. The correlation between Figures 2  
155 and 3a is 0.55 (see Table 1), which shows that there is significant correlation, but also significant  
156 variability between the two estimates of top-heaviness. With a very conservative (less conserva-  
157 tive) assumption of 20 (100) degrees of freedom, 0.43 (0.19) would be a statistically significant  
158 correlation at the 95 percent level. Given the uncertainties in moist physics parameterization in  
159 the reanalysis and the difficulty simulating mean precipitation patterns in numerical models, the  
160 agreement between these methodologies on what regions are top-heavy is very noteworthy, despite  
161 being far from perfect.

162 Figure 3b shows the top-heaviness ratio estimated using idealized basis functions rather than  
163 reanalysis-derived basis functions. In this case, the first basis function is half a sine wave extending  
164 from 1000hPa to 100hPa, and the second basis function is a full sine wave extending over the same  
165 depth. The fields shown in Figure 3a and 3b are closely correlated with a correlation coefficient  
166 of 0.94, showing that the broad-scale patterns in Figure 3a are not due to details of the reanalysis-  
167 derived basis functions. This supports the robustness of results and usefulness of our methodology  
168 for estimating top-heaviness. It shows that our best estimate of top-heaviness from satellite data,  
169 shown in 3a is not strongly influenced by reanalysis.

## 170 *b. Rain Type*

171 Geographic variations in stratiform rain fraction (the fraction of the total rain falling in regions  
172 identified by radar as being stratiform) have been posited to be related to vertical motion top-  
173 heaviness (e.g. Schumacher et al. 2004; Houze 2004). Stratiform rain in this context is defined by  
174 how it appears on radar: fairly homogeneous in the horizontal with a layered structure on vertical

175 cross sections. It often has a “bright band” or layer of high reflectivity in which ice particles  
176 are melting (Houze 1997). This is contrasted with convective precipitation which has “cells” or  
177 horizontally localized patches or cores of intense radar reflectivity. In field campaigns, times  
178 with high stratiform rain fraction have been observed to correspond to times with more top-heavy  
179 vertical motion profiles (e.g. Houze 1989). However, it has also been noted that the heating profiles  
180 associated with convective rain are less consistent from case to case (Houze 1989).

181 Figure 4a shows stratiform rain fraction as seen by TRMM 3A25 in regions where precipitation  
182 is greater than 5mm per day. The 5mm/day threshold was chosen as a round number that covers a  
183 similar geographic area to the regions where upward vertical motion occurs (that this must be the  
184 case can be shown using variants on methods in HB). Stratiform rain in the TRMM 3A25 product is  
185 identified using a variant of the method developed by Steiner et al. (1995) according to the readme  
186 file (TRMM 2016b). The method judges whether a pixel is convective by comparing its reflectivity  
187 to that of an average intensity taken over a surrounding background. If the pixels intensity exceeds  
188 the surrounding background by a factor,  $f$ , the pixel is considered to be convective. The threshold  
189  $f$  depends on the background intensity, where the background intensity is the average reflectivity  
190 over some region. The functional form of  $f$  as a function of background intensity is calibrated to  
191 match a manual separation of convective and stratiform regions in regions where it is possible to  
192 identify a bright band. A bright band is considered a sufficient but not necessary condition for a  
193 region to be stratiform, as bright bands are not always seen regions considered stratiform. Hence,  
194 the local intensity compared to background intensity is used to identify convective regions and the  
195 remaining regions are considered stratiform. Note that the vertical structure of the reflectivity is  
196 not directly used to estimate stratiform rain fraction, so the stratiform rain fraction metric does not  
197 directly provide information on vertical motion top-heaviness.

198 The stratiform rain fraction in Figure 4a generally varies between 0.35 and 0.55 with most val-  
199 ues in the center of that range. The region with highest stratiform rain fraction is in the eastern  
200 Pacific region where vertical motion profiles are bottom-heavy according to the metrics shown  
201 in Figure 2 and Figure 3. Higher values of stratiform rain fraction tend to also occur in the At-  
202 lantic, Western Pacific and some of the Indian Ocean. Lower values occur in the Southern Pacific  
203 Convergence Zone (SPCZ) the south-eastern Atlantic ITCZ and north of 5N, 45-95W. Note that  
204 there is no relationship between regions of high stratiform rain fraction and regions with top-heavy  
205 (or bottom-heavy) vertical motion profiles. Correlation coefficients between figures are shown in  
206 Table 1 for regions where data is shown in all previous figures. The part of the Pacific that has  
207 the most bottom-heavy vertical motion profiles, the central-eastern Pacific, has comparatively high  
208 stratiform rain fraction, above 0.5. This may seem surprising based on the arguments advanced in  
209 some earlier work (e.g. Schumacher et al. 2004; Houze 2004) that regions with more stratiform  
210 rain fraction are more top-heavy. We discuss this finding and the relationship to existing studies  
211 further, below, after examining shallow and convective rain fraction maps.

212 Climatological shallow rain fraction in regions with greater than 5mm per day rainfall is shown  
213 in Fig 4b. This quantity generally varies between 0.05 and 0.15 in deep convective regions. The  
214 regions with the largest shallow rain fractions are in the central-eastern Pacific ITCZ and on the  
215 eastern edge of the SPCZ. Lower shallow rain fractions occur in the western Pacific and around  
216 the maritime continent. They also occur in the eastern Pacific warm pool region. The larger  
217 shallow rain fraction in the central-eastern Pacific ITCZ is consistent with vertical motion in this  
218 region being more bottom-heavy and in general shallow rain fraction appears to be higher where  
219 other metrics suggest more bottom-heavy vertical motion profiles. However, the overall shallow  
220 rain fraction, as well as its variations are small enough that the dramatic vertical motion profile

221 variations can't be explained by this alone. Hence, the result that top-heaviness is not correlated  
222 with stratiform rain fraction cannot be explained by variations in shallow rain fraction alone.

223 Deep convective rain fraction (i.e. not including shallow rain) in these regions is shown in  
224 Fig 4c. This quantity generally varies between 0.25 and 0.4. Comparatively low convective rain  
225 fraction occurs over the northern central-eastern Pacific ITCZ (210-240E), in the west Pacific  
226 (130-160E) and over the northern part of the Atlantic ocean. As seen in previous figures, these  
227 regions have quite varied vertical motion profiles ranging from quite bottom-heavy to quite top-  
228 heavy. This may be because the shape of the convective latent heating profile varies geographically  
229 due to geographic variations in the depth of the convection in these regions. Back and Bretherton  
230 (2009a,b) elucidated reasons for variations in the depth of convection. Geographic variations in  
231 convective heating profiles are consistent with the fact that ground-based observations have shown  
232 that vertical motions in convective regions are variable, as noted in Houze (1989).

### 233 **3. Why stratiform rain fraction may not explain top-heaviness**

234 Returning to the seemingly surprising result that stratiform rain fraction is not correlated with  
235 top-heaviness, we now discuss how this can be reconciled with existing literature on this subject.  
236 Ground-based observations are generally considered more reliable than satellite data, and these  
237 show stratiform profiles are more top-heavy (e.g. Houze 1989) than convective heating profiles.  
238 Our results are not contradicting that finding. In fact, we examined the top-heaviness ratio used  
239 here as a function of stratiform rain fraction in the region where the Tropical Global Ocean Atmo-  
240 sphere Coupled Ocean-Atmosphere Response Experiment (TOGA-COARE Webster and Lukas  
241 1992) took place and found that top-heaviness (satellite-derived and reanalysis) in that region in-  
242 creases monotonically when binned by stratiform rain fraction (not shown). However, if there is  
243 any significant variability within convective heating profiles, as there may be from region to region,

244 the well-known finding does not necessarily imply that a larger stratiform rain fraction must be  
 245 associated with more top-heavy vertical motion profiles. Mathematically, this insight comes from  
 246 the fact that stratiform and convective heating profiles do not need to be orthogonal as described  
 247 below.

248 An illustrative counter-example to the common view (as in Schumacher et al. 2004) that regions  
 249 with higher stratiform rain fraction are more top-heavy is shown in Figure 5. The first panel shows  
 250 the contributions to vertical motion of a hypothetical top-heavy convective heating profile, and a  
 251 hypothetical stratiform profile, as well as the sum of the two, for a case with stratiform rain fraction  
 252 0.3. The second panel shows contributions to vertical motion of a hypothetical bottom-heavy  
 253 heating profile, with stratiform rain fraction 0.5. We describe how this figure was constructed  
 254 below. It illustrates that it is possible for higher stratiform rain fraction to be associated with a  
 255 more bottom-heavy vertical motion profile if convective heating profiles vary enough.

256 To construct each subpanel in this figure, we use a linear system of 4 equations. The unknowns  
 257 in the equation are amplitudes of convective and stratiform  $\Omega_i$ . We denote the convective vertical  
 258 motion profiles:

$$\omega_c(p, x) = o_{1,c}(x)\Omega_1(p) + o_{2,c}(x)\Omega_2(p) \quad (7)$$

259 and stratiform vertical motion:

$$\omega_s(p, x) = o_{1,s}(x)\Omega_1(p) + o_{2,s}(x)\Omega_2(p) \quad (8)$$

260 We assume total rainfall (due to convective plus stratiform vertical motion) in both cases is 10  
 261 mm/day and radiative cooling corresponds to 5 mm/day of precipitation (these are reasonable  
 262 values for the ITCZ). Working from equation 3, this gives us an equation for overall rainfall (the  
 263 same equation for both panels):

$$L'10mm/day = M_{s1} * (o_{1,c} + o_{1,s}) + M_{s2} * (o_{2,c} + o_{2,s}) - L'5mm/day \quad (9)$$

264  $L'$  is the latent heat of condensation divided by the number of seconds in a day. In the top-heavy  
 265 left hand panel, the total vertical motion motion top-heaviness ratio is 0.4, while this measure is  
 266 -0.4 in the bottom-heavy right hand panel. This gives us a second equation for both cases. For the  
 267 top-heavy case, this is:

$$\frac{o_{2,c} + o_{2,s}}{o_{1,c} + o_{1,s}} = 0.4 \quad (10)$$

268 For the bottom-heavy case -0.4 is substituted for 0.4. In both cases, the top-heaviness ratio of the  
 269 vertical motion associated with stratiform rain is assumed to be the same: 1.1. This gives us a third  
 270 equation:

$$\frac{o_{2,s}}{o_{1,s}} = 1.1; \quad (11)$$

271 The fourth equation comes from the stratiform rain fraction. For this equation, we need to make  
 272 an assumption about how much of the precipitation associated with radiative cooling is stratiform  
 273 precipitation. We assume this fraction is the same as the overall stratiform rain fraction, but the  
 274 nature of the figures is not particularly sensitive to this assumption. For the top-heavy case with  
 275 stratiform rain fraction 0.3, this yields the following equation for stratiform rainfall:

$$L'0.3 * 10mm/day = M_{s1}o_{1,s} + M_{s2}o_{2,s} - L'0.3 * 5mm/day \quad (12)$$

276 For the bottom-heavy case 0.5 is substituted in for 0.3 as the stratiform rain fraction. We solve the  
 277 corresponding linear system of equations to find the convective and stratiform profiles shown.

278 The second panel of Figure 5ab has more stratiform vertical motion (67% more) and the strat-  
 279 iform profiles are always much more top-heavy than convective heating profiles in this example.  
 280 However the variations in the shape of the convective heating profiles between the two panels are  
 281 more than large enough to make up for the variations in stratiform heating amount and hence the  
 282 overall heating profile is significantly more top-heavy in the first case. This example demonstrates  
 283 that stratiform heating profiles can be more top-heavy than convective heating profiles everywhere,

284 without this implying that a higher stratiform rain fraction must be associated with more top-heavy  
285 profiles.

286 Another possible factor contributing to the lack of correlation between stratiform rain fraction  
287 and top-heaviness is that the heating profiles associated with what is identified as stratiform re-  
288 gions are varying geographically. Houze et al. (2015) described scenes identified by the TRMM  
289 2A23 algorithm as stratiform that consist of “closely spaced, weak and shallow vertically oriented  
290 echoes or cells” and have a “faint, but nearly continuous bright band [that] extends horizontally  
291 across the region of weak cells” (see their Figure 12bdfh). They noted that it is doubtful that these  
292 types of stratiform regions have heating profiles like those associated with the stratiform regions  
293 of mesoscale convective systems (MCS) and posited that the cellular stratiform echoes in ITCZ  
294 regions may be associated with a shallow overturning mode. Also, (Houze 1989) showed some  
295 variations in the height of maximum heating and relative amplitude between top heating and bot-  
296 tom heating/cooling in stratiform precipitation regions (see their Figures 16-18). Hence variations  
297 in stratiform heating profiles could contribute to the finding that stratiform rain fraction is not  
298 correlated with top-heaviness.

299 Stratiform rain fraction is measured only when it is raining, while vertical motion top-heaviness  
300 integrates over both raining and non-raining times. This might be argued to be an additional  
301 issue with the idea that stratiform rain fraction explains vertical motion profiles. However, as  
302 equation 3 makes clear, there is a direct relationship between the amount of vertical motion and  
303 the rainfall, provided radiative cooling varies little. Hence, vertical motion is also to first order  
304 effectively “weighted” by rainfall, e.g. the vertical motion profiles that contribute more to rainfall  
305 also contribute more to overall vertical motion. Thus it makes sense from that perspective to  
306 compare stratiform rain fraction and top-heaviness ratio as we have done, rather than utilizing a  
307 precipitation-weighted top-heaviness ratio.

308 Overall, our results clearly warn that one should not always assume higher stratiform rain frac-  
309 tions are associated with more top-heavy vertical motion profiles (even if shallow heating is com-  
310 parable).

#### 311 **4. Conclusions**

312 We introduced a new methodology for visualizing geographic variability in the climatological  
313 top-heaviness of vertical motion profiles in deeply convecting regions using reanalysis data. This  
314 reanalysis top-heaviness was compared to that estimated using the satellite-based methodology  
315 of Handlos and Back (2014). The reanalysis and satellite-based methodologies agree on which  
316 regions are more top-heavy or bottom-heavy, but the satellite-based methodology tends to produce  
317 larger variations from bottom-heavy to top-heavy vertical motion profiles. Notably, climatological  
318 stratiform rain fraction as measured by TRMM was not correlated with top-heaviness or bottom-  
319 heaviness, at odds with what some past studies have posited. Shallow rain fraction variations were  
320 not large enough to explain the major variations in top-heaviness. The lack of relationship be-  
321 tween stratiform rain fraction and top-heaviness is likely due to either a) geographic variations in  
322 the depth of convective heating profiles and/or b) variations in stratiform heating profiles, poten-  
323 tially associated with “cellular” type stratiform heating profiles substantially different than MCS  
324 stratiform heating.

325 A notable result in this study and other findings (e.g. Back and Bretherton 2006) is that the  
326 Eastern Pacific ITCZ has bottom-heavy vertical motion profiles but high stratiform rain fraction  
327 values (e.g. Schumacher et al. 2004). This suggests that deep convection is behaving differently in  
328 this region than has been documented in previous field campaigns. Back and Bretherton (2009b)  
329 argued that the bottom-heavy vertical motion profiles exist due to strong SST gradients in this  
330 region and relatively low SST. This may lead to either very bottom-heavy convective heating

331 profiles (as in Fig 5b), and/or stratiform heating associated with weak convection that doesn't  
332 go very deep. Finding out which of these possibilities (or others) is going on is worthy of further  
333 study. As described in the introduction, this has implications for retrieval and understanding of  
334 latent heating and vertical profiles from satellite data. This suggests that a field campaign in the  
335 Eastern Pacific ITCZ that could shed light on this issue would have broad utility.

336 *Acknowledgments.* This research was supported by NASA Grant NNX12AL96G and NSF Grant  
337 MSN188169. Thanks to Kuniaki Inoue for coming up with the idea to produce Figure 1b. The  
338 comments of Matthew Igel and two anonymous reviewers have improved the manuscript.

### 339 **References**

- 340 Adam, O., T. Bischoff, and T. Schneider, 2016: Seasonal and interannual variations in the energy  
341 flux equator and itcz. part ii: Zonally varying shifts in the itcz. *J. Climate*, **submitted**.
- 342 Back, L. E., and C. S. Bretherton, 2006: Geographic variability in the export of moist static  
343 energy and vertical motion profiles in the tropical pacific. *Geophysical Research Letters*, **33 (17)**,  
344 L17 810.
- 345 Back, L. E., and C. S. Bretherton, 2009a: On the relationship between sst gradients, boundary  
346 layer winds, and convergence over the tropical oceans. *Journal of Climate*, **22 (15)**, 4182–4196.
- 347 Back, L. E., and C. S. Bretherton, 2009b: A simple model of climatological rainfall and vertical  
348 motion patterns over the tropical oceans. *Journal of Climate*, **22 (23)**, 6477–6497.
- 349 Bretherton, C. S., and P. K. Smolarkiewicz, 1989: Gravity waves, compensating subsidence and  
350 detrainment around cumulus clouds. *Journal of the Atmospheric Sciences*, **46 (6)**, 740–759.
- 351 Charney, J. G., 1963: A note on large-scale motions in the tropics. *Journal of the Atmospheric*  
352 *Sciences*, **20 (6)**, 607–609.

- 353 Dee, D. P., and Coauthors, 2011: The era-interim reanalysis: Configuration and performance of  
354 the data assimilation system. *Quarterly Journal of the Royal Meteorological Society*, **137 (656)**,  
355 553–597.
- 356 Frierson, D. M., and Coauthors, 2013: Contribution of ocean overturning circulation to tropical  
357 rainfall peak in the northern hemisphere. *Nature Geoscience*, **6 (11)**, 940–944.
- 358 Grecu, M., and W. S. Olson, 2006: Bayesian Estimation of Precipitation from Satellite Passive  
359 Microwave Observations Using Combined Radar – Radiometer Retrievals. *Journal of Applied*  
360 *Meteorology and Climatology*, **45**, 416–433.
- 361 Grecu, M., W. S. Olson, C. L. Shie, T. S. L’Ecuyer, and W. K. Tao, 2009: Combining satellite  
362 microwave radiometer and radar observations to estimate atmospheric heating profiles. *Journal*  
363 *of Climate*, **22 (23)**, 6356–6376.
- 364 Handlos, Z. J., and L. E. Back, 2014: Estimating vertical motion profile shape within tropical  
365 weather states over the oceans. *Journal of Climate*, **27 (20)**, 7667–7686.
- 366 Hartmann, D., H. Hendon., and J. R.A. Houze, 1984: Some implications of the mesoscale cir-  
367 culations in cloud clusters for large-scale dynamics and climate, j. *Journal of the Atmospheric*  
368 *Sciences*, **41**, 113– 121.
- 369 Houze, R. A., 1989: Observed structure of mesoscale convective systems and implications for  
370 large-scale heating. *Quarterly Journal of the Royal Meteorological Society*, **115 (487)**, 425–  
371 461.
- 372 Houze, R. A., 2004: Mesoscale convective systems. *Reviews of Geophysics*, **42 (4)**, RG4003.

- 373 Houze, R. A., K. L. Rasmussen, M. D. Zuluaga, and S. R. Brodzik, 2015: The variable nature of  
374 convection in the tropics and subtropics: A legacy of 16 years of the tropical rainfall measuring  
375 mission satellite. *Reviews of Geophysics*, **53** (3), 994–1021.
- 376 Houze, R. A. J., 1997: Stratiform precipitation in regions of convection: A meteorological para-  
377 dox? *Bulletin of the American Meteorological Society*, **78** (10), 2179–2196.
- 378 Kang, S. M., D. M. W. Frierson, and I. M. Held, 2009: The tropical response to extratropical  
379 thermal forcing in an idealized gcm: The importance of radiative feedbacks and convective  
380 parameterization. *Journal of the Atmospheric Sciences*, **66** (9), 2812–2827.
- 381 L'ecuyer, T. S., and G. Mcgarragh, 2010: A 10-year climatology of tropical radiative heating and  
382 its vertical structure from trmm observations. *Journal of Climate*, **23** (3), 519–541.
- 383 L'Ecuyer, T. S., and G. L. Stephens, 2003: The tropical oceanic energy budget from the TRMM  
384 perspective. Part I: Algorithm and uncertainties. *Journal of Climate*, **16** (12), 1967–1985.
- 385 L'Ecuyer, T. S., and G. L. Stephens, 2007: The tropical atmospheric energy budget from the  
386 TRMM perspective. Part II: Evaluating GCM representations of the sensitivity of regional en-  
387 ergy and water cycles to the 1998-99 ENSO cycle. *Journal of Climate*, **20** (18), 4548–4571.
- 388 North, G. R., T. L. Bell, and R. F. Cahalan, 1982: Sampling Errors in the Estimation of Empirical  
389 Orthogonal Functions. *Monthly Weather Review*, **110** (7), 699–706.
- 390 Schneider, T., T. Bischoff, and G. H. Haug, 2014: Migrations and dynamics of the intertropical  
391 convergence zone. *Nature*, **513** (7516), 45–53.
- 392 Schumacher, C., J. R. A. Houze, and I. Kraucunas, 2004: The tropical dynamical response to latent  
393 heating estimates derived from the trmm precipitation radar. *J. Atmos. Sci.*, **61**, 1341–1358.

394 Sherwood, S. C., S. Bony, and J.-L. L. Dufresne, 2014: Spread in model climate sensitivity traced  
395 to atmospheric convective mixing. *Nature*, **505 (7481)**, 37–42.

396 Sobel, A. H., and C. S. Bretherton, 2000: Modeling tropical precipitation in a single column.  
397 *Journal of Climate*, **13 (24)**, 4378–4392.

398 Steiner, M., R. A. Houze Jr, and S. E. Yuter, 1995: Climatological characterization of three-  
399 dimensional storm structure from operational radar and rain gauge data. *Journal of Applied*  
400 *Meteorology*, **34 (9)**, 1978–2007.

401 TRMM, ., 2016a: Readme for trmm product 3b42 (v7). URL [http://disc.sci.gsfc.nasa.gov/  
402 precipitation/documentation/TRMM\\_README/TRMM\\_3B42\\_readme.shtml](http://disc.sci.gsfc.nasa.gov/precipitation/documentation/TRMM_README/TRMM_3B42_readme.shtml).

403 TRMM, ., 2016b: Trmm product level 2a precipitation radar (pr) rain characteristics (2a23).

404 Webster, P. J., and R. Lukas, 1992: Toga coare: The coupled oceanatmosphere response experi-  
405 ment. *Bulletin of the American Meteorological Society*, **73 (9)**, 1377–1416.

406 Wu, Z., E. S. Sarachik, and D. S. Battisti, 2000: Vertical structure of convective heating and the  
407 three-dimensional structure of the forced circulation on an equatorial beta plane\*. *Journal of the*  
408 *atmospheric sciences*, **57 (13)**, 2169–2187.

409 Yanai, M., S. Esbensen, and J.-H. Chu, 1973: Determination of bulk properties of tropical cloud  
410 clusters from large-scale heat and moisture budgets. *Journal of the Atmospheric Sciences*, **30 (4)**,  
411 611–627.

412 **LIST OF TABLES**

413 **Table 1.** The correlation coefficients and RMS difference (in parentheses, where rele-  
414 vant) between quantities shown in Figures 2, 3ab, 4abc in regions where rainfall  
415 is greater than 5 mm/day. . . . . 22

	Reanalysis o2/o1	Satellite o2/o1	Idealized Basis fn Satellite o2/o1
Reanalysis o2/o1	1.0	0.55 (0.013)	0.63 (0.014)
Satellite o2/o1	0.55 (0.013)	1.0	0.94 (0.004)
Idealized Basis fn Satellite o2/o1	0.63 (0.014)	0.94 (0.004)	1.0
Stratiform Rain Fraction	-0.18	-0.13	-0.15
Shallow Rain Fraction	-0.36	-0.59	-0.57
Convective Rain Fraction	-0.04	-0.24	-0.21

416 TABLE 1. The correlation coefficients and RMS difference (in parentheses, where relevant) between quantities  
417 shown in Figures 2, 3ab, 4abc in regions where rainfall is greater than 5 mm/day.

418 **LIST OF FIGURES**

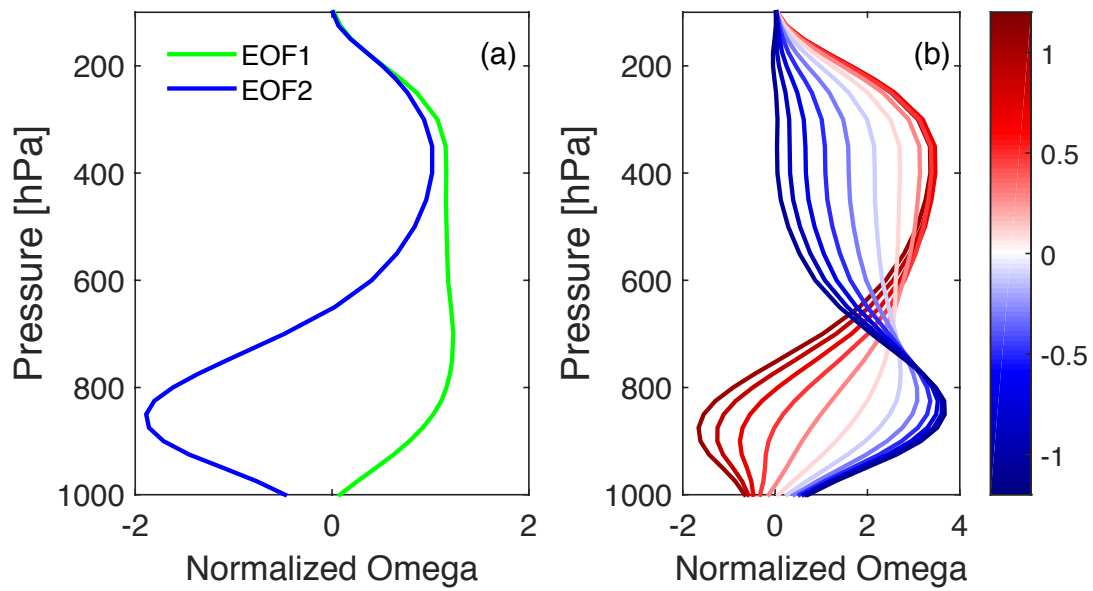
419 **Fig. 1.** a) First two empirical orthogonal functions (EOFs) from a principal component analysis of  
 420 vertical motion profile variability as a function of height. b) Vertical motion profile shapes  
 421 constructed from given “top-heaviness” ratios of EOF 2 to EOF 1. Colors correspond to  
 422 those in Figure 2. . . . . 24

423 **Fig. 2.** Climatological top-heaviness ratio (mean amplitude of second principal component to mean  
 424 amplitude of first principal component), as a function of location in reanalysis. This figure  
 425 utilizes the analysis used to derive EOFs in Figure 1). Colors correspond to vertical motion  
 426 profile shapes shown in Figure 1b. . . . . 25

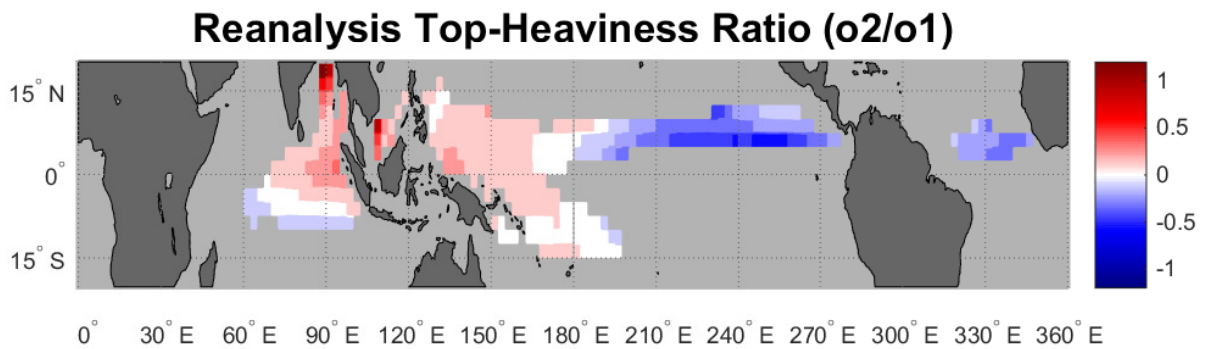
427 **Fig. 3.** a) Top-heaviness ratio as in Figure 4, estimated from satellite data, using the methodology  
 428 of Handlos and Back (2014) with basis functions shown in Figure 1. b) Utilizes sinusoidal  
 429 basis functions and the same methodology; shows that overall patterns are not sensitive to  
 430 basis function choice. Color-scale saturates at both ends. . . . . 26

431 **Fig. 4.** Climatological stratiform rain fraction (a), shallow rain fraction (b) and deep convective rain  
 432 fraction (c) in regions where precipitation is greater than 5mm per day from TRMM 3A25  
 433 product. Color-scale saturates at both ends . . . . . 27

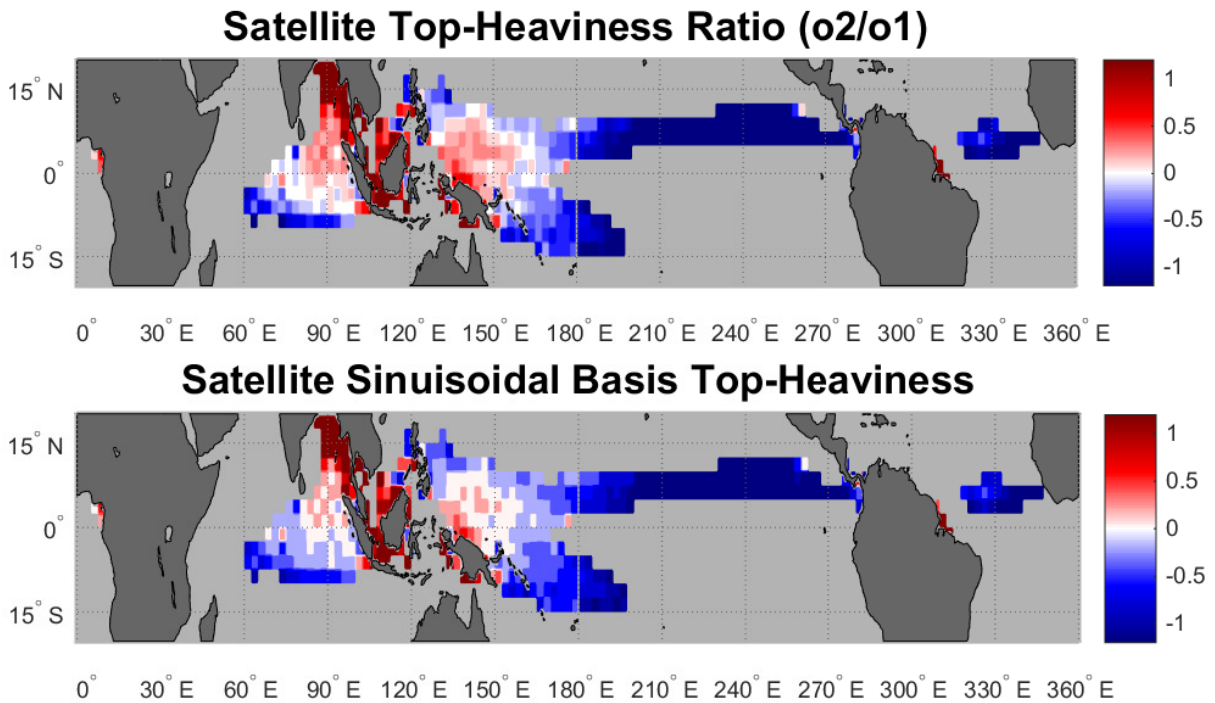
434 **Fig. 5.** An example of how geographically varying convective heating profiles can lead to stratiform  
 435 rain fraction not being correlated with top-heaviness. Left panel (a) shows hypothetical  
 436 example for top-heavy region of the contribution of convective and stratiform vertical motion  
 437 to the total profile, as well as total profile (sum of the convective, stratiform profiles). Right  
 438 panel (b) shows hypothetical example for a bottom-heavy region. Stratiform rain fraction is  
 439 higher (0.55) in right hand panel compared to left hand panel (0.35). See text for details. . . . 28



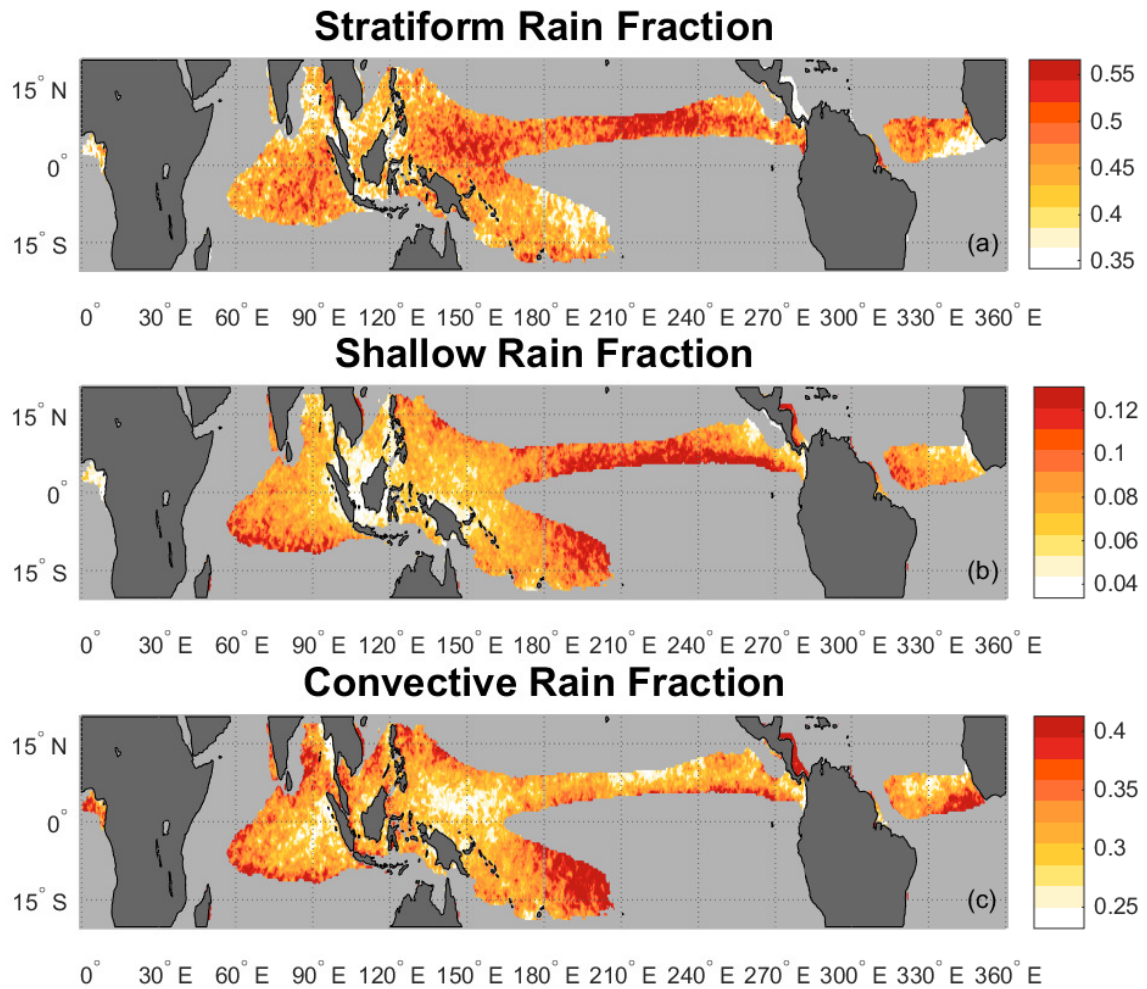
440 FIG. 1. a) First two empirical orthogonal functions (EOFs) from a principal component analysis of vertical  
 441 motion profile variability as a function of height. b) Vertical motion profile shapes constructed from given  
 442 “top-heaviness” ratios of EOF 2 to EOF 1. Colors correspond to those in Figure 2.



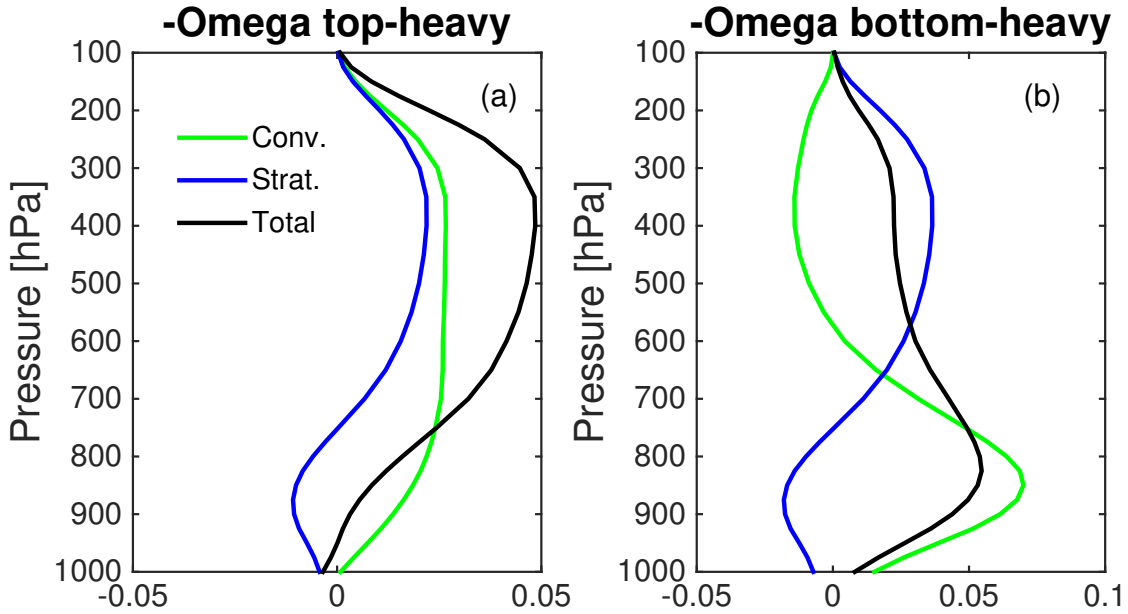
443 FIG. 2. Climatological top-heaviness ratio (mean amplitude of second principal component to mean amplitude  
 444 of first principal component), as a function of location in reanalysis. This figure utilizes the analysis used to  
 445 derive EOFs in Figure 1). Colors correspond to vertical motion profile shapes shown in Figure 1b.



446 FIG. 3. a) Top-heaviness ratio as in Figure 4, estimated from satellite data, using the methodology of Handlos  
 447 and Back (2014) with basis functions shown in Figure 1. b) Utilizes sinuisoidal basis functions and the same  
 448 methodology; shows that overall patterns are not sensitive to basis function choice. Color-scale saturates at both  
 449 ends.



450 FIG. 4. Climatological stratiform rain fraction (a), shallow rain fraction (b) and deep convective rain fraction  
 451 (c) in regions where precipitation is greater than 5mm per day from TRMM 3A25 product. Color-scale saturates  
 452 at both ends



453 FIG. 5. An example of how geographically varying convective heating profiles can lead to stratiform rain  
 454 fraction not being correlated with top-heaviness. Left panel (a) shows hypothetical example for top-heavy region  
 455 of the contribution of convective and stratiform vertical motion to the total profile, as well as total profile (sum  
 456 of the convective, stratiform profiles). Right panel (b) shows hypothetical example for a bottom-heavy region.  
 457 Stratiform rain fraction is higher (0.55) in right hand panel compared to left hand panel (0.35). See text for  
 458 details.